Distributions of Tropical Precipitation Cluster Power and Their Changes under Global Warming. Part I: Observational Baseline and Comparison to a High-Resolution Atmospheric Model

KEVIN M. QUINN AND J. DAVID NEELIN

Department of Atmospheric and Oceanic Sciences, University of California, Los Angeles, Los Angeles, California

(Manuscript received 20 September 2016, in final form 2 June 2017)

ABSTRACT

The total amount of precipitation integrated across a precipitation feature (contiguous precipitating grid cells exceeding a minimum rain rate) is a useful measure of the aggregate size of the disturbance, expressed as the rate of water mass lost or latent heat released (i.e., the power of the disturbance). The probability distribution of cluster power is examined over the tropics using Tropical Rainfall Measuring Mission (TRMM) 3B42 satellite-retrieved rain rates and global climate model output. Observed distributions are scale-free from the smallest clusters up to a cutoff scale at high cluster power, after which the probability drops rapidly. After establishing an observational baseline, precipitation from the High Resolution Atmospheric Model (HiRAM) at two horizontal grid spacings (roughly 0.5° and 0.25°) is compared. When low rain rates are excluded by choosing a minimum rain-rate threshold in defining clusters, the model accurately reproduces observed cluster power statistics at both resolutions. Middle and end-of-century cluster power distributions are investigated in HiRAM in simulations with prescribed sea surface temperatures and greenhouse gas concentrations from a ''business as usual'' global warming scenario. The probability of high cluster power events increases strongly by end of century, exceeding a factor of 10 for the highest power events for which statistics can be computed. Clausius–Clapeyron scaling accounts for only a fraction of the increased probability of high cluster power events.

1. Introduction

Extremes of precipitation intensity are projected to change across all global warming scenarios in phases 3 and 5 of the Coupled Model Intercomparison Project (CMIP3 and CMIP5) experiments (Tebaldi et al. 2006; Kharin et al. 2007, 2013; O'Gorman and Schneider 2009; Sillmann et al. 2013a,b). Tebaldi et al. (2006) review historical and future simulations from a suite of nine coupled global climate models across multiple emissions scenarios, finding a clear signal of increased precipitation intensity emerging by end of century over the globe. Kharin et al. (2007, 2013) also analyze a suite of coupled climate models for consistency in projections of extreme precipitation spanning the CMIP3 and CMIP5 experiments, finding shorter wait times for extreme precipitation events by end of century relative to historical climate and that the intensity of extreme precipitation events increases at a rate of 6% $°C^{-1}$ of warming across both CMIP3 and CMIP5 experiments. Additionally, Sillmann et al. (2013b) find that several metrics of precipitation extremes increase proportional to warming.

Uncertainties regarding changes in precipitation extremes emerge in both observations (e.g., Easterling et al. 2000; Alexander et al. 2006; Kharin et al. 2007, 2013; Lenderink and van Meijgaard 2008; Allan et al. 2010) and in global-scale simulations of extreme precipitation in recent climate and future climate (e.g., Tebaldi et al. 2006; Kharin et al. 2007, 2013; Allan and Soden 2008; Allan et al. 2010; Sillmann et al. 2013a,b). Kharin et al. (2007) hypothesize that, over the tropics, uncertainty in simulated extreme precipitation results from limitations in the representation of associated

Denotes content that is immediately available upon publication as open access.

Supplemental information related to this paper is available at the Journals Online website: http://dx.doi.org/10.1175/JCLI-D-16-0683.s1.

Corresponding author: Kevin M. Quinn, kquinn@atmos.ucla.edu

DOI: 10.1175/JCLI-D-16-0683.1

physical processes in climate models. Additionally, simulated precipitation extremes from an ensemble of 19 CMIP3 models are lower than observed precipitation extremes from 1987–2004 (Allan and Soden 2008). Chen and Knutson (2008) note that, when considering extreme precipitation events, modeled precipitation should be analyzed as areal averages versus point estimates. At regional scales, a survey of climate model studies using multiple approaches (e.g., multimodel ensembles and downscaling) suggests that projected changes to extreme precipitation event frequency and intensity also exhibit large regional variability (e.g., Beniston et al. 2007; Kay and Washington 2008; Seneviratne et al. 2012; Vizy and Cook 2012; Haensler et al. 2013; IPCC 2013, 2014; Sylla et al. 2015).

Characterizing changes in the frequency and intensity of organized convection, including in tropical cyclones, is important because of their potential socioeconomic impacts. Many studies into tropical cyclone changes under global warming suggest that overall global tropical cyclone frequency will decrease by end of century (e.g., Emanuel et al. 2008; Knutson et al. 2008, 2010, 2013; Bender et al. 2010), though tropical cyclone intensity is projected to increase, both measured by higher rain rates and hurricane category (e.g., Webster et al. 2005; Emanuel et al. 2008; Gualdi et al. 2008; Knutson et al. 2008, 2013; Bender et al. 2010). Changes in tropical cyclone intensity under global warming are further investigated in climate model simulations by Knutson et al. (2013), Villarini et al. (2014), and Wehner et al. (2015). Decreases in the total number of tropical cyclones but increases in intense tropical cyclones in future climate under global warming are described in Knutson et al. (2013) and Wehner et al. (2015). Rainfall rates associated with tropical cyclones are projected to increase (Knutson et al. 2013; Villarini et al. 2014; Wehner et al. 2015), scaling with the Clausius–Clapeyron (CC) relationship in some regions (Knutson et al. 2013; Villarini et al. 2014), but exceeding results expected under CC scaling near centers of tropical cyclones (Knutson et al. 2013; Wehner et al. 2015). More generally, changes in convective organization, as noted in observations by Tan et al. (2015), may be important to changes in precipitation extremes.

Work to better understand processes of convective organization (e.g., Leary and Houze 1979; Houze 1982; Houze 1989; Mapes and Houze 1993; Houze 2004) in current climate includes studies of the self-aggregation of tropical convection over smaller domains (e.g., Bretherton et al. 2005; Muller and Held 2012; Khairoutdinov and Emanuel 2013; Wing and Emanuel 2014; Wing and Cronin 2016). The aggregation of convection into clusters has been shown to be sensitive to: hydrometeor parameterization (Bretherton et al. 2005); Coriolis forcing (Bretherton et al. 2005); low cloud distribution (Muller and Held 2012); SST changes (Khairoutdinov and Emanuel 2013); and advection of moist static energy (Wing and Cronin 2016). Additionally, Wing and Emanuel (2014) note that processes that initiate the aggregation of convective cells into clusters (e.g., atmospheric water vapor absorbing shortwave radiation and surface heat flux) are different than processes that maintain aggregation once it has already occurred (e.g., longwave radiation feedback). Cluster aggregation processes at smaller scales appear to continue into idealized large domains in modeling studies (Holloway et al. 2012; Bretherton and Khairoutdinov 2015; Arnold and Randall 2015).

Observational studies of tropical precipitation clusters over large domains include Mapes et al. (2009), Peters et al. (2009, 2010, 2012), Wood and Field (2011), and Skok et al. (2013). In Skok et al. (2013), space–time clusters are defined to analyze precipitation statistics associated with tropical cyclones, using satellite-retrieved precipitation estimates from the Tropical Rainfall Measuring Mission (TRMM) 3B42 data. Mapes et al. (2009) examines cluster life cycle and size distributions using IR and scatterometer datasets over the tropics, noting that small clusters with brief lifespans constitute the vast majority of oceanic storm clusters. Wood and Field (2011) and Peters et al. (2009, 2010, 2012) analyze storm cluster organization using a variety of observational datasets, noting that probability distributions of cluster cloud area (Peters et al. 2009; Wood and Field 2011), precipitation integrated across contiguous precipitating clusters [cluster power (Peters et al. 2012)] or precipitation accumulations [precipitation integrated across temporal events (Peters et al. 2010)] follow a long, scale-free power law, with a distinct cutoff (i.e., a more rapid drop in frequency of occurrence) at large cluster area and high power. Cluster power behavior above the cutoff is different than behavior below the cutoff, in part because different physical processes drive daily tropical convection and tropical cyclones (Peters et al. 2012). Furthermore, Peters et al. (2012) noted that tropical cyclones provide significant contributions to the tail in the large event regime. Neelin et al. (2017) find changes in end-of-century precipitation accumulations, especially for changes in probability of the very largest accumulations. This is associated with the form of the distribution, and in particular with the physics that determines how the cutoff scale changes with warming, motivating examination here of analogous behavior for spatial clusters.

There is a need for the validation of rainfall simulations in climate models, especially extreme events in quantities likely important for changes under global warming, such as measures of organized convection. Distributions of precipitation integrated across a cluster over the tropics are thus examined here for the first time as (i) a potentially useful measure both as a metric of model simulation in current climate and (ii) as a measure of changes in tropical disturbances in simulations of future climate. This integrated precipitation can be described as cluster power (defined here as the instantaneous latent heat release integrated over a cluster of contiguous precipitating grid cells). Distributions and tail sensitivity to the most powerful storm clusters at a global scale are examined in satellite observations with full spatial coverage and compared to climate model simulations for the first time, examining the relationship between cluster power and rain rate across a global domain. We first establish an observational baseline using satellite-retrieved precipitation data to test its usefulness for comparison to climate model output at two resolutions. Second, we assess how reliably a high-resolution climate model can simulate historical cluster power distributions. Last, we apply output from future runs of the same model to examine mid- and end-of-century simulated cluster power distributions, quantifying the influence of global warming on cluster power behavior. These results for a high-resolution model set the stage for further examination of lower-resolution coupled models from the CMIP5 archive in Quinn and Neelin (2017, hereafter Part II).

2. Data and methods

Satellite-retrieved rain-rate data from the TRMM 3B42 program are used to build a baseline of cluster power behavior. Data from sensors onboard the TRMM spacecraft are merged with data from other satellites to provide gap-free TRMM 3B42 rain-rate data over oceans and land and are available beginning in 1998 (Huffman et al. 2007; TRMM 2015). These data have units of millimeters per hour and are available every three hours over a $0.25° \times 0.25°$ latitude–longitude grid. For consistency with our comparisons in Part II, we analyze twice daily TRMM 3B42 time slices at 0000 and 1200 UTC. To calculate cluster power, precipitating grid cells meeting a minimum rain-rate threshold are first aggregated into distinct clusters. From there, cluster power is expressed as the instantaneous latent heat release integrated over a cluster in units of gigawatts by multiplying rain rates by the latent heat of condensation ($2.5 \times 10^6\,\mathrm{J\,kg^{-1}}$), which relates cluster power to the earth's energy budget. Cluster power can also be expressed equivalently in terms of a mass budget as the integrated mass of water lost per hour ($\mathrm{kg\,H_2O\,h^{-1}}$) with 1 GW equal to $1.4 \times 10^6\,\mathrm{kg\,H_2O\,h^{-1}}$ lost.

Precipitation data from the Geophysical Fluid Dynamics Laboratory (GFDL) High Resolution Atmospheric Model (HiRAM) at two horizontal resolutions are incorporated into this study: 25 (HiRAM-C360) and 50 km (HiRAM-C180) (Zhao et al. 2009, 2010; Chen and Lin 2011; Held and Zhao 2011; Zhao and Held 2010, 2012; Merlis et al. 2013; Villarini et al. 2014; GFDL 2015). HiRAM output is derived from the historical Atmospheric Model Intercomparison Project [AMIP (1979–2008)] and future [SST2030 (2026–35) and SST2090 (2086–95)] experiments, incorporating prescribed sea surface temperatures (SSTs) from the Met Office Hadley Centre Sea Ice and SST version 1.1 model (Rayner et al. 2003) for the historical period, and greenhouse gas and SST anomalies from the GFDL Earth System Model, version 2 (GFDL-ESM2), for future runs. Precipitation data are given at 3 h intervals in units of precipitation flux ($\mathrm{kg\,m^{-2}\,s^{-1}}$), though to stay consistent with the TRMM 3B42 retrieval, instantaneous HiRAM cluster power snapshots from only 0000 and 1200 UTC with rain rates meeting a minimum threshold are aggregated into distinct clusters. These clusters then have their rate of water mass loss converted to instantaneous latent heat release, using the same method as the TRMM 3B42 dataset. Next, we compare AMIP simulation output with satellite-retrieved data to assess its accuracy in simulating historical conditions. After establishing an accurate AMIP baseline, we then use these AMIP simulations for the comparison with future climate simulations, with C360 data directly compared to observed data because of their comparable spatial resolution.

The binning procedure in building probability density functions (PDFs) for these distributions is as follows. One wants to have bin width increase smoothly as probabilities drop, for which a bin width that is approximately constant in log space is suitable. It is important also to recognize that the increments of cluster size are quantized to multiples of the minimum cluster size. To ensure that the bin spacing is consistent with this, bin widths are adjusted to the integer multiple of the minimum cluster size that is closest to the asymptotic constant bin width chosen for the upper end of the distribution. In practice, the variations in bin are small; Table 1 of the supplementary information shows both bin width and histogram counts N_i prior to normalization by the width of bin i and the total counts for each analysis presented. Error bars are given by $\pm N_i^{1/2}$, with the same normalization as the PDF. The minimum cluster size is set by the grid size and the minimum precipitation threshold, so the same bin boundaries apply to historical and future climate runs of the same dataset. Cluster power distributions for 1 May–30 September are shown over a global tropics domain from 30°S to 30°N. To illustrate the extent to which cluster power behavior is influenced by domain size, a northern Atlantic–eastern Pacific domain, extending from the equator to 30°N and from 140°W across the Americas and Atlantic Ocean to 0°, is shown in the supplementary information. Cluster power distributions were also examined over other domains, yielding similar results.

3. Analysis

a. Cluster power distributions: Observations

Previous cluster studies have analyzed cluster quantities such as cloud area above a certain reflectivity threshold (Wood and Field 2011), storm cluster area and duration using IR imagery and scatterometer data (Mapes et al. 2009), and cluster area and power using satellite radar and passive microwave imagery (Peters et al. 2009, 2012). In the case of radar imagery, these have been for narrow swaths, limited by the radar swath width. In Fig. 1, we form an observational baseline for cluster power using satellite-retrieved rain-rate data, evaluating the merged satellite TRMM 3B42 retrieval at a global scale over land and ocean, so statistics are not limited by swath width. Figure 1 examines TRMM 3B42 cluster power distributions for multiple rain-rate thresholds at a global scale.

Across the tropics at multiple rain-rate thresholds (Fig. 1), TRMM 3B42 cluster power distributions follow a long, scale-free power law, similar to that in Peters et al. (2012), who noted an exponent of −1.87 in the TRMM radar 2A25 retrieval. The exponent here (as estimated from the slope of the least squares best-fit line over the power-law range at the 0.7 $\mathrm{mm\,h^{-1}}$ rain-rate threshold in Fig. 1) is −1.50. In Fig. 1, the cutoff that terminates the power-law range for all rain-rate thresholds lies at approximately 10^5 GW, with the frequency of the highest power clusters for all distributions falling off more rapidly after the cutoff. This cutoff also appears to be insensitive to rain-rate threshold. Note that the cluster power of the lowest power bin depends on rain-rate threshold, simply because the minimum cluster power is a function of the minimum rain rate considered and the gridcell size. Cluster power distributions must begin at a threshold-dependent minimum power and are shifted slightly because this affects the normalization of the probability distribution.

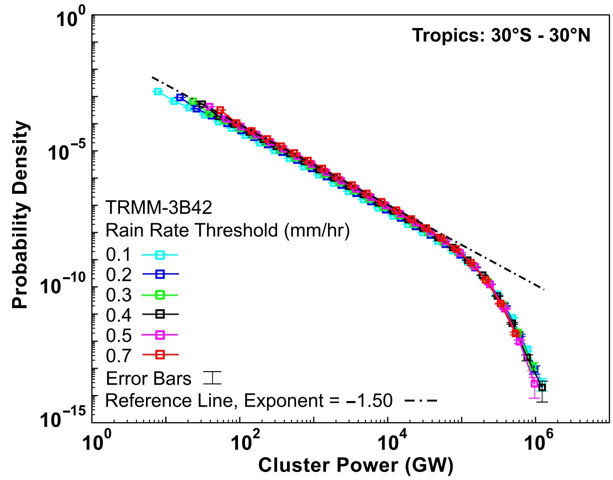

FIG. 1. Probability distributions of cluster power (i.e., precipitation integrated over clusters of contiguous pixels exceeding the specified rain-rate threshold) expressed in units of latent heat release (GW), with 1 GW equivalent to $1.4 \times 10^6\,\mathrm{kg\,H_2O\,h^{-1}}$ in integrated precipitation. Clusters are calculated from the TRMM 3B42 precipitation product, over the tropics, May–September 1998–2008. The least squares best-fit exponent before the cutoff (fit over the scale-free range up to 10^5 GW for the 0.7 $\mathrm{mm\,h^{-1}}$ threshold) is −1.50.

To provide further context for this distribution, Fig. S1 in supplemental information (SI) shows the distribution of cluster area [previously examined in other datasets by Mapes and Houze (1993) and Peters et al. (2009)], which likewise exhibits an approximate power-law range followed by a reduction in probability above the cutoff scale. The cutoff scale for area is more dependent on the rain-rate threshold than that for power. The total rate of water loss from the cluster is a physically important quantity, so here we focus on cluster power. To provide a sense of how the cluster power distribution might change if evaluated over a particular subset of the tropics, Fig. S2 in the SI shows comparable results for the Atlantic–eastern Pacific region. The power-law range has a similar exponent (−1.42 vs −1.50), and the cutoff occurs at a similar power.

Intriguingly, the form of the cluster power probability distribution is similar to what occurs for temporal clusters (i.e., accumulations of precipitation over events) in a simple prototype model (Stechmann and Neelin 2011, 2014; Neelin et al. 2017) that also exhibits a power-law range with approximately exponential cutoff. The exponent of that simple configuration, −1.5, is close to the exponent for precipitation integrated over spatial clusters here. An apparent exponent of −1.2 or steeper, depending on convective parameters, was noted for the power-law range in cluster area distributions in a similar simple model (Hottovy and Stechmann 2015), but no

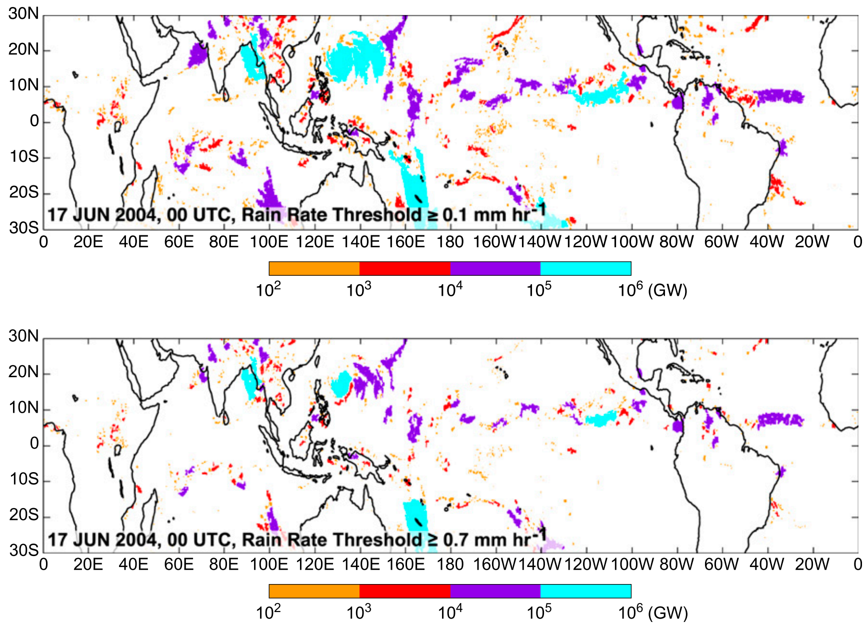

FIG. 2. Examples of precipitation clusters from the selected TRMM 3B42 time slice for rain-rate thresholds of (top) 0.1 and (bottom) 0.7 mm h^{-1}. The spatial distribution of each cluster is shown with the power integrated over the cluster given by the legend.

quantitative prototype appears to exist yet for integrated cluster precipitation. For continuity with previous literature, probability distributions for cluster area are shown for reference in Fig. S1. Similar to the power distributions, an approximately power-law range is found for cluster area, extending from the minimum area (7×10^8 m^2) to a qualitatively similar cutoff at around 3×10^{11} m^2, with an exponent of approximately -1.7. The cutoff for area distributions exhibits slightly more dependence on rain-rate threshold. We choose the integrated precipitation–power for the cluster for the remainder of this work because of its greater physical importance as a result of the correspondence to total water loss–latent heat release from the cluster.

Figure 2 displays typical satellite-retrieved cluster morphology at the lowest and highest minimum rain-rate thresholds considered in this study (0.1 and 0.7 mm h^{-1}) for a sample day in 2004. Most clusters at the 0.1 mm h^{-1} rain-rate threshold with high cluster power ($\geq 10^5$ GW) resemble tropical cyclones, mesoscale convective systems, ITCZ-like features, or the tail ends of midlatitude fronts that occasionally pass between 20° and 30°N and between 20° and 30°S. At the 0.7 mm h^{-1} rain-rate threshold, the overall structure of most features remains the same, with only some trimming on the edges of the largest features. These examples of cluster morphology are provided simply to illustrate the phenomena that are being condensed into the distributions and provide a sense of why little variation in cluster power behavior across rain-rate thresholds occurs in the observational distributions.

b. *Cluster power distributions: Historical HiRAM output*

Figures 3–5 quantify how the HiRAM at two horizontal resolutions approximates observed cluster power behavior. Figure 3 compares HiRAM cluster power distributions at multiple rain-rate thresholds, while Fig. 4 displays HiRAM distributions at two resolutions. Figure 5 overlays HiRAM-C360 and TRMM 3B42 cluster power distributions at two rain-rate thresholds.

Like the TRMM 3B42 dataset (Fig. 1), HiRAM cluster power distributions (Figs. 3,4) are also scale-free along a power-law range, have a cutoff around 10^5 GW, and display little sensitivity to rain-rate threshold along the power-law range before the cutoff. Additionally, HiRAM distribution least squares best-fit exponents (for the 0.7 mm h^{-1} threshold) range from -1.36 to -1.39 (depending on horizontal resolution), similar to the TRMM 3B42 analysis (-1.50, Fig. 1). The lower-resolution simulation (HiRAM-C180) has a shorter scale-free region because of coarser resolution resulting in a larger minimum cluster area and hence larger minimum cluster power. The HiRAM-C180 PDF is slightly farther from the observations in the sense that probability density drops slightly less steeply than that of C360. Otherwise, its

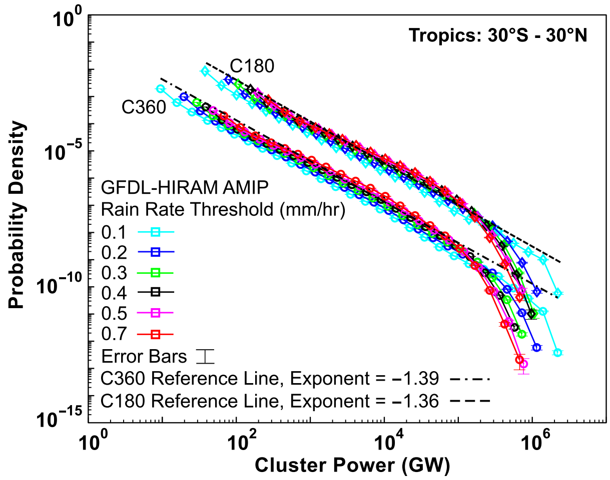

FIG. 3. As in Fig. 1, but for GFDL HiRAM AMIP simulations at two resolutions (C180 and C360). For readability, HiRAM-C180 AMIP distributions have been shifted up vertically by a decade. The least squares best-fit exponent before the cutoff is −1.36 for HiRAM-C180 and −1.39 for HiRAM-C360.

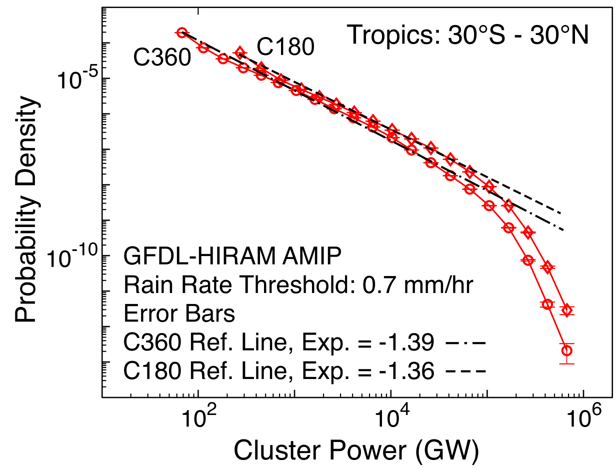

FIG. 4. As in Fig. 3, but comparing modeled cluster power probability distributions between resolutions for the 0.7 mm h^{-1} rain-rate threshold, with no vertical shift of the HiRAM-C180 distribution. Note that the normalization differs simply because the coarse-resolution model does not extend to as small a minimum cluster size.

scale-free power-law range and cutoff closely parallel that from the higher-resolution simulation (Fig. 4).

Tail behavior sensitivity to rain-rate threshold is quantified in Fig. 3. While TRMM 3B42 distributions exhibit little sensitivity, HiRAM distributions do exhibit substantial sensitivity above the cutoff for low rain-rate thresholds. At rain-rate thresholds below 0.3 mm h^{-1}, the cutoff shifts toward higher power. This finding is consistent with previous findings that global climate models can overestimate light precipitation coverage (e.g., Dai 2006). Beginning at a rain-rate threshold of 0.3 mm h^{-1} and above, tails of the distributions converge, suggesting that it is important to exclude low rain rates from clusters and that higher minimum rain-rate thresholds are more robust for comparison with observations. For an illustration of the spatial behavior of modeled precipitation clusters, refer to Figs. S3 and S4 in the SI.

The comparison between TRMM 3B42 and HiRAM-C360 cluster power distributions in Fig. 6 shows that, in general, the tail of the modeled power distribution at the 0.7 mm h^{-1} rain-rate threshold more closely parallels the TRMM 3B42 distribution. Although their least squares best-fit exponents are slightly different [−1.39 for HiRAM-C360 (Fig. 3) and −1.50 for TRMM 3B42 in (Fig. 1)] and the tail of the TRMM 3B42 distribution is longer, the tails for both distributions at high power are very similar.

We also ask how HiRAM-C360 cluster power distributions compare to distributions from a synthetic time series created from the same data that deliberately removes any spatial relations beyond those that would occur from the climatological probability of precipitation (Fig. 5). Clusters can occur even in simple systems in which there is no spatial correlation and

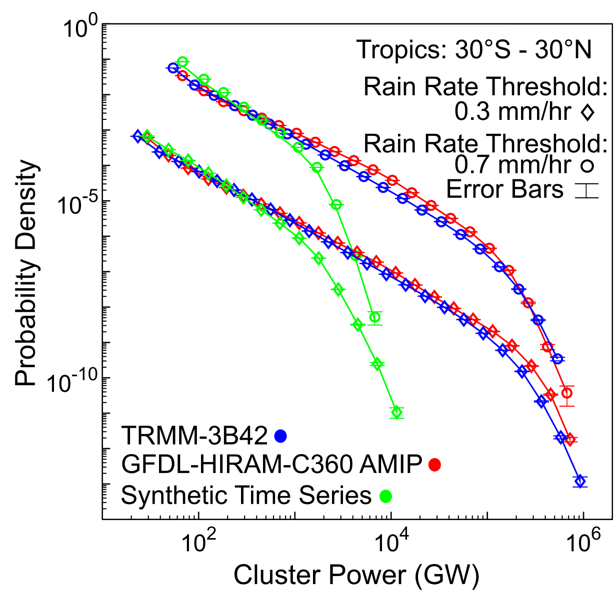

FIG. 5. Observed (TRMM 3B42) and modeled (HiRAM-C360 AMIP) tropics cluster power probability distributions for May–September 1998–2008 for rain-rate thresholds 0.3 and 0.7 mm h^{-1}. Also plotted are cluster probability distributions at each rain-rate threshold from a synthetic time series created by random selections from 1979–99 HiRAM-C360 AMIP data that preserve probability distributions at each point but not spatial correlations (see text). The distributions for the 0.7 mm h^{-1} rain-rate threshold have been shifted up vertically by two decades to improve readability.

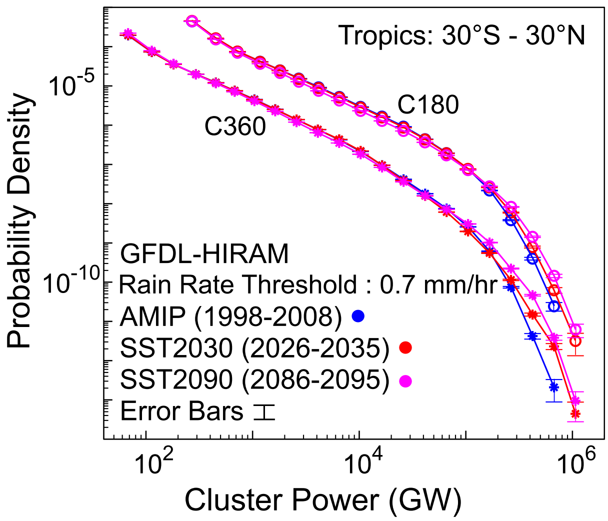

FIG. 6. As in Fig. 3, but displaying a comparison of HiRAM cluster power probability distributions at two resolutions for historical (AMIP, May–September 1998–2008) and future (SST2030 and 2090, May–September 2026–35 and 2086–95, respectively) simulations for the 0.7 mm h^{-1} rain-rate threshold. HiRAM-C180 cluster power distributions have been shifted up vertically by a decade for readability.

under certain circumstances these can have power-law distributions [Stauffer and Aharony (1994); for discussion in a meteorological context see, e.g., Peters et al. (2009)]—due diligence thus requires that we verify that the reproduction of observed cluster distributions by HiRAM is well distinguished from such a simple case. The synthetic time series is analogous to a statistical null hypothesis model, in that strong differences between HiRAM-C360 cluster power distributions and those of the synthetic time series provide evidence that spatial relations simulated dynamically in the model are key to producing the PDF. To build the synthetic time series that preserves rain-rate probabilities while artificially removing these spatial relations, we select rain-rate values for each grid cell from random time steps at the same spatial location using HiRAM-C360 data from 1 May–30 September 1979–99. The rain-rate probabilities as a function of space are preserved, but all other spatial autocorrelation effects are destroyed. Clusters are then evaluated from the synthetic time series at rain-rate thresholds of 0.3 and 0.7 mm h^{-1} just as for the actual HiRAM-C360 output, and the PDFs are compared. The synthetic time series distributions clearly have different structures than the observed–HiRAM distributions; the power-law range, if present, is too short to be clearly seen, and distinct cutoffs occur at relatively low cluster power. This comparison suggests that the features of the observed cluster PDF captured by HiRAM are not obtained just by chance occurrence of neighboring raining points.

c. Cluster power distributions: Future HiRAM output

Changes in the frequency of high cluster power events (e.g., tropical cyclones) may have large societal repercussions. As a result, we examine changes in future cluster power distributions (Figs. 6, 7) by comparing historical (AMIP), midcentury (SST2030), and end-of-century (SST2090) cluster power distributions at the 0.7 mm h^{-1} rain-rate threshold used in this study. Historical, midcentury, and end-of-century distributions are very similar to each other before the cutoff, following the same long, scale-free power-law range (Fig. 6). By end of century, there is a clear signal in both simulations that indicates a shift toward higher power in the tail region, implying more frequent intense storm clusters (Fig. 6). This increase (for the highest three bins for which statistics can be calculated, which span a factor of 4 in storm power: 2–8 $\times$ 10^{5} GW) is a factor of approximately 3, 10, and almost 20, respectively, as indicated on Fig. 7a for the highest-resolution simulation by end of century. Figure 7b shows an alternate means of displaying this information as a form of risk ratio (Otto et al. 2012): specifically, showing the ratio of the probability density. This increases rapidly for the largest cluster sizes, similar to time-domain results for accumulations (Neelin et al. 2017), which exhibited an approximately exponential increase for the largest accumulations. The end of century also has events of unprecedented size, as may be seen in Fig. 7a, but these are not shown in Fig. 7b since they would be estimated as infinite ratio. Figure 7b also shows a test of robustness of the binning procedure, showing two cases with slightly smaller asymptotic bin widths, for which the last bin with nonzero counts in the historical period is shifted by approximately half a bin width and almost one bin width, respectively. These yield highly consistent results over the portion of the curve that they estimate. Additionally, if instead of considering changes to the probabilities of fixed bins, we consider how the tail of the distribution extends, the probability corresponding to the highest power bin in the historical period shifts to higher power: for the end of century, this probability occurs for a power that has increased by roughly a factor of 1.4 relative to current climate (Fig. 7a).

Other studies (e.g., Knutson et al. 2013; Villarini et al. 2014; Wehner et al. 2015) have compared changes in modeled rain rates under global warming scenarios with changes expected under CC scaling of humidity, so to test a possible physical explanation for the increased probability of intense storm clusters by end of century,

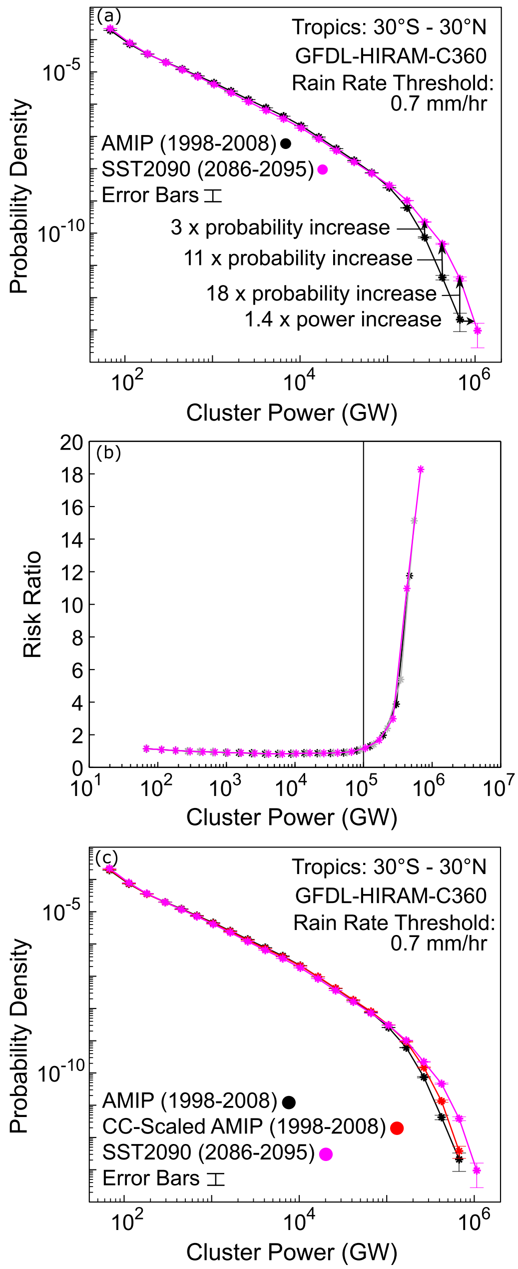

FIG. 7. (a) As in Fig. 6, but for the change in the distribution of cluster power between historical (AMIP) and future (SST2090) simulations for the 0.7mm h^{-1} rain-rate threshold using the higher-resolution HiRAM (C360), with probability increase factors displayed for selected bins above the cutoff (vertical arrows). Horizontal arrow shows the estimated power increase for the probability value at the highest bin that can be estimated in current climate. (b) The change in cluster power distribution displayed as a risk ratio of the probability density for the end of century to that in the historical period. Magenta line shows the risk ratio as estimated from the curves in (a); black and gray curves show tests of sensitivity to alternate bin-width choices: asymptotic bin widths of 0.1920 (black) and 0.1960 (gray). (c) Black and magenta curves are as in Fig. 7a, with an additional comparison (red) to the AMIP dataset with a CC-scaling factor applied (see text).

we examine changes to cluster power distributions under a realistic global warming scenario. The difference in mean global temperature between HiRAM-C360 SST2090 and AMIP experiments is +2.16 K, within the range of temperature increase projected by IPCC (2013). Assuming a 7% increase in specific humidity per 1-K warming under the CC relationship, this represents a possible 15.12% increase in precipitation under global warming. Given this warming, we multiply HiRAM-C360 AMIP rain rates (at the 0.7 mm h^{-1} threshold) by a factor of 1.15, recluster (keeping the same threshold), and then reanalyze this CC-scaled dataset, comparing its distribution of cluster power to HiRAM-C360 AMIP and SST2090 distributions.

The application of a CC-scaling factor to the HiRAM-C360 AMIP dataset does increase frequency of the most powerful storm clusters and shift the tail region of the CC-scaled dataset toward higher power compared to the original HiRAM-C360 AMIP dataset (Fig. 7c). However, this application appears to only account for a fraction of the increased probability of the most intense storm clusters, suggesting that the increased probability of the most intense storm clusters by end of century is significantly higher than that expected based on a simple CC scaling of precipitation intensity. Knutson et al. (2013) and Wehner et al. (2015) also found that rain-rate increases surrounding the cores (e.g., within 200 km) of intense tropical cyclones under global warming exceed rain-rate increases that would be expected solely under CC scaling of precipitation, hypothesizing a link between this exceedance and the dynamics driving the intensity around the cores of intense tropical cyclones. Wang et al. (2015) also note a link between an increase in precipitation rates near storm centers, CC scaling, and the dynamics affecting the convergence near storm centers. In a different study, Knutson et al. (2015) find that, where end-of-century SST increases are particularly large, though not uniform globally, the amount of precipitation associated with intense hurricanes also increases at a rate exceeding CC scaling of precipitation. Although detailed analysis of spatial structures is beyond the scope of this work, Fig. S4 provides examples of storms from the large-power end of the distribution for reference.

4. Summary and discussion

Observed cluster power distributions are found to follow a long, scale-free power law between 10 and 10^5 GW, with a rapid drop off in the frequency of storm clusters with high cluster power thereafter. In units of mass loss, the cutoff near 10^5 GW is equivalent to approximately 10^{11} kg h^{-1}. The phenomena leading to these clusters range from convective phenomena at the gridcell scale (approximately 25 km) and mesoscale clusters through ITCZ disturbances and tropical cyclones. The cutoff at high power is largely independent of rain rate in the observations, and here is found in a dataset not limited by swath width, or land versus ocean retrievals. This suggests that some set of physical factors within the tropical climate system and the meteorology of storm aggregation must lead to the existence of the cutoff, as further discussed below.

HiRAM simulations at both resolutions for the historical period accurately reproduce observed distributions using a minimum rain-rate threshold of 0.7 mm h^{-1}, with similar least squares best-fit exponents over the power-law range (−1.5 for TRMM 3B42 and −1.39 and −1.36 for HiRAM-C360 and HiRAM-C180, respectively). At both model resolutions, the cutoff at high power is correctly produced near 10^5 GW, suggesting that model resolution has little impact on simulating cluster power. HiRAM cutoff values are sensitive to rain-rate threshold, as a result of the overly widespread occurrence of low rain rates, but agree well provided the threshold is not too low.

A first step in posing the question of what processes might be important to this distribution shape is to ask whether the HiRAM simulation of the atmospheric dynamics driving the aggregation of neighboring contiguous precipitating grid cells can be distinguished from simpler processes that might be hypothesized to account for some of the effects. The simplest process that can create clusters potentially exhibiting such a distribution, including a power-law range under certain circumstances, would be one in which precipitation occurs with observed probabilities but without the dynamical information of spatial relations. Constructing a synthetic time series from the HiRAM-C360 data but with the spatial relation between grid cells destroyed by randomizing the time step from which the rain-rate sample is drawn provides a simple foil that acts like a null hypothesis. The cluster power distributions resulting from the synthetic time series are quantitatively well distinguished from the observed and HiRAM distributions. This verifies that the atmospheric dynamics driving cluster distributions in HiRAM are more complex than simply yielding reasonable probabilities of precipitation.

The long scale-free range in both observations and HiRAM but not in the simplest case tested by the synthetic time series suggests that the length and slope of the scale-free range, as well as the apparent change of dynamical regimes at the cutoff, constitute interesting targets for explanation in modeling of cluster aggregation. Theory has recently been developed for the distribution of precipitation accumulation—the integral of precipitation over the time for which it exceeds a specified threshold—which is the analog in the time domain of the cluster power integrated over spatially continuous points. The accumulation distribution with a power-law range followed by a roughly exponential cutoff seen in observations (Peters et al. 2010) and models (Neelin et al. 2017) can be mimicked by stochastic models for the prognostic column moisture equation (Stechmann and Neelin 2014; Neelin et al. 2017). In the time domain case, fluctuations of moisture convergence drive variations of moisture, with the time derivative of moisture providing a memory of previous states. Precipitation accumulation corresponds to the physical effect of the integrated loss of moisture. The cutoff scale is set by the interplay between the magnitude of the moisture convergence fluctuations and the integrated loss and thus increases under global warming as moisture convergence fluctuations increase (Neelin et al. 2017). Creating analogous theory for the spatial case is desirable but is a nontrivial undertaking, given the complex processes creating horizontal relations between neighboring columns, including moisture transport by convergent and rotational components of the flow, gravity wave dynamics, and radiative interactions. We conjecture that model experiments in idealized domains or with interventions in model dynamics that have been used to study various aspects of aggregation (e.g., Bretherton et al. 2005; Muller and Held 2012; Holloway et al. 2012; Khairoutdinov and Emanuel 2013; Wing and Emanuel 2014; Wing and Cronin 2016; Bretherton and Khairoutdinov 2015; Arnold and Randall 2015) might feasibly be used to determine if the cutoff scale found here corresponds to any fundamental physical scale of the system.

Because the cutoff affects the probability of the highest cluster power events, potentially very important for human impacts, changes to cluster power distributions under global warming are examined. HiRAM cluster power distributions at both resolutions from the future SST2030 and SST2090 experiments have the same long, scale-free range as historical HiRAM output, but the cutoff tends to shift toward higher power. A natural simple hypothesis to compare against for the increased probability of more intense storms by end of century is a CC scaling of the precipitation to factor in the simplest impacts of temperature on specific humidity. Specifically, a CC-scaling factor of 7% increase per degree of warming under the projected change to mean global temperature (2.16 K, calculated using HiRAM-C360 AMIP and SST2090 temperature data) was applied to the HiRAM-C360 AMIP dataset before running the same clustering and binning procedures. The resulting cluster power distribution with this hypothetical CC-scaled precipitation lies between the original AMIP and SST2090 cluster power distributions, indicating that the change in future cluster power distributions considerably exceeds expectations based on a simple CC scaling of rain rates.

The shift of the cutoff toward higher cluster power in the warmer climate has a substantial impact on the frequency of occurrence of the largest storms. The probability of high cluster power events for the end of century relative to the historical period increases rapidly beyond the historical cutoff. These increases substantially exceed a factor of 10 for the highest bin for which cluster power statistics can be computed in the historical period. Phrased another way, at the corresponding value of probability for the highest bin in which statistics can be computed for the historical period, the end of century clusters would be roughly 40% more powerful.

Acknowledgments. This project was supported in part by the National Science Foundation (NSF Grant AGS-1540518) and National Oceanic and Atmospheric Administration (NOAA Grants NA14OAR4310274 and NA15OAR4310097). Portions of this material have been presented at the 96th Annual Meeting of the American Meteorological Society and the 49th Fall Meeting of the American Geophysical Union in 2016 and have formed part of the 2016 UCLA Ph.D. thesis of K. M. Quinn. We thank the National Aeronautics and Space Administration (NASA) and Japan Aerospace Exploration Agency (JAXA) for producing their observational precipitation data sets (available at https://disc.gsfc.nasa.gov/datacollection/TRMM_3B42_7.html). Additionally, we would like to acknowledge the NOAA/Geophysical Fluid Dynamics Laboratory (GFDL) for producing their model output (available at http://nomads.gfdl.noaa.gov:8080/DataPortal/cmip5.jsp). We thank N. Berg, K. Hales-Garcia, M. Schwartz, and D. Walton for assistance in procedure development and J. Meyerson for graphics support.

REFERENCES

Alexander, L. V., and Coauthors, 2006: Global observed changes in daily extremes of temperature and precipitation. *J. Geophys. Res.*, **111**, D05109, doi:10.1029/2005JD006290.

Allan, R. P., and B. J. Soden, 2008: Atmospheric warming and the amplification of precipitation extremes. *Science*, **321**, 1481–1484, doi:10.1126/science.1160787.

——, ——, V. O. John, W. Ingram, and P. Good, 2010: Current changes in tropical precipitation. *Environ. Res. Lett.*, **5**, 025205, doi:10.1088/1748-9326/5/2/025205.

Arnold, N. P., and D. A. Randall, 2015: Global-scale convective aggregation: Implications for the Madden–Julian oscillation. *J. Adv. Model. Earth Syst.*, **7**, 1499–1518, doi:10.1002/2015MS000498.

Bender, M. A., T. R. Knutson, R. E. Tuleya, J. J. Sirutis, G. A. Vecchi, S. T. Garner, and I. M. Held, 2010: Modeled impact of anthropogenic warming on the frequency of intense Atlantic hurricanes. *Science*, **327**, 454–458, doi:10.1126/science.1180568.

Beniston, M., and Coauthors, 2007: Future extreme events in European climate: An exploration of regional climate model projections. *Climatic Change*, **81**, 71–95, doi:10.1007/s10584-006-9226-z.

Bretherton, C. S., and M. Khairoutdinov, 2015: Convective self-aggregation feedbacks in near-global cloud-resolving simulations of an aquaplanet. *J. Adv. Model. Earth Syst.*, **7**, 1765–1787, doi:10.1002/2015MS000499.

——, P. N. Blossey, and M. Khairoutdinov, 2005: An energy-balance analysis of deep convective self-aggregation above uniform SST. *J. Atmos. Sci.*, **62**, 4273–4292, doi:10.1175/JAS3614.1.

Chen, C.-T., and T. Knutson, 2008: On the verification and comparison of extreme rainfall indices from climate models. *J. Climate*, **21**, 1605–1621, doi:10.1175/2007JCLI1494.1.

Chen, J. H., and S. J. Lin, 2011: The remarkable predictability of inter-annual variability of Atlantic hurricanes during the past decade. *Geophys. Res. Lett.*, **38**, L11804, doi:10.1029/2011GL047629.

Dai, A., 2006: Precipitation characteristics in eighteen coupled climate models. *J. Climate*, **19**, 4605–4630, doi:10.1175/JCLI3884.1.

Easterling, D. R., G. A. Meehl, C. Parmesan, S. A. Chagnon, T. R. Karl, and L. O. Mearns, 2000: Climate extremes: Observations, modeling, and impacts. *Science*, **289**, 2068–2074, doi:10.1126/science.289.5487.2068.

Emanuel, K. A., R. Sundararajan, and J. Williams, 2008: Hurricanes and global warming: Results from downscaling IPCC AR4 simulations. *Bull. Amer. Meteor. Soc.*, **89**, 347–367, doi:10.1175/BAMS-89-3-347.

GFDL, 2015: Global atmospheric models. Accessed 30 November 2015. [Available online at http://www.gfdl.noaa.gov/atmospheric-model.]

Gualdi, S., E. Soccimarro, and A. Navarra, 2008: Changes in tropical cyclone activity due to global warming: Results from a high-resolution coupled general circulation model. *J. Climate*, **21**, 5204–5228, doi:10.1175/2008JCLI1921.1.

Haensler, A., F. Saeed, and D. Jacob, 2013: Assessing the robustness of projected precipitation changes over central Africa on the basis of a multitude of global and regional climate projections. *Climatic Change*, **121**, 349–363, doi:10.1007/s10584-013-0863-8.

Held, I. M., and M. Zhao, 2011: The response of tropical cyclone statistics to an increase in CO_2 with fixed sea surface temperatures. *J. Climate*, **24**, 5353–5364, doi:10.1175/JCLI-D-11-00050.1.

Holloway, C. E., S. J. Woolnough, and G. M. Lister, 2012: Precipitation distributions for explicit versus parametrized convection in a large-domain high-resolution tropical case study. *Quart. J. Roy. Meteor. Soc.*, **138**, 1692–1708, doi:10.1002/qj.1903.

Hottovy, S., and S. N. Stechmann, 2015: A spatiotemporal stochastic model for tropical precipitation and water vapor dynamics. *J. Atmos. Sci.*, **72**, 4721–4738, doi:10.1175/JAS-D-15-0119.1.

Houze, R. A., Jr., 1982: Cloud clusters and large-scale vertical motions in the tropics. *J. Meteor. Soc. Japan*, **60**, 396–410, doi:10.2151/jmsj1965.60.1_396.

——, 1989: Observed structure of mesoscale convective systems and implications for large-scale heating. *Quart. J. Roy. Meteor. Soc.*, **115**, 425–461, doi:10.1002/qj.49711548702.

——, 2004: Mesoscale convective systems. *Rev. Geophys.*, **42**, RG4003, doi:10.1029/2004RG000150.

Huffman, G. J., and Coauthors, 2007: The TRMM Multisatellite Precipitation Analysis (TMPA): Quasi-global, multiyear, combined-sensor precipitation estimates at fine scales. *J. Hydrometeor.*, **8**, 38–55, doi:10.1175/JHM560.1.

IPCC, 2013: *Climate Change 2013: The Physical Science Basis*. Cambridge University Press, 1535 pp.

——, 2014: *Climate Change 2014: Impacts, Adaptation, and Vulnerability. Part B: Regional Aspects*. Cambridge University Press, 688 pp. [Available online at http://www.ipcc.ch/pdf/assessment-report/ar5/wg2/WGIIAR5-PartB_FINAL.pdf.]

Kay, G., and R. Washington, 2008: Future southern African summer rainfall variability related to a southwest Indian Ocean dipole in HadCM3. *Geophys. Res. Lett.*, **35**, L12701, doi:10.1029/2008GL034180.

Khairoutdinov, M., and K. A. Emanuel, 2013: Rotating radiative-convective equilibrium simulated by a cloud-resolving model. *J. Adv. Model. Earth Syst.*, **5**, 816–825, doi:10.1002/2013MS000253.

Kharin, V. V., F. W. Zwiers, X. Zhang, and G. C. Hegerl, 2007: Changes in temperature and precipitation extremes in the IPCC ensemble of global coupled model simulations. *J. Climate*, **20**, 1419–1444, doi:10.1175/JCLI4066.1.

——, ——, ——, and M. F. Wehner, 2013: Changes in temperature and precipitation extremes in the CMIP5 ensemble. *Climatic Change*, **119**, 345–357, doi:10.1007/s10584-013-0705-8.

Knutson, T. R., J. J. Sirutis, S. T. Garner, G. A. Vecchi, and I. M. Held, 2008: Simulated reduction in Atlantic hurricane frequency under twenty-first-century warming conditions. *Nat. Geosci.*, **1**, 359–364, doi:10.1038/ngeo202.

——, and Coauthors, 2010: Tropical cyclones and climate change. *Nat. Geosci.*, **3**, 157–163, doi:10.1038/ngeo779.

——, and Coauthors, 2013: Dynamical downscaling projections of twenty-first-century Atlantic hurricane activity: CMIP3 and CMIP5 model-based scenarios. *J. Climate*, **26**, 6591–6617, doi:10.1175/JCLI-D-12-00539.1.

——, J. Sirutis, M. Zhao, R. Tuleya, M. Bender, G. Vecchi, G. Villarini, and D. Chavas, 2015: Global projections of intense tropical cyclone activity for the late twenty-first century from dynamical downscaling of CMIP5/RCP4.5 scenarios. *J. Climate*, **28**, 7203–7224, doi:10.1175/JCLI-D-15-0129.1.

Leary, C. A., and R. A. Houze, 1979: The structure and evolution of convection in a tropical cloud cluster. *J. Atmos. Sci.*, **36**, 437–457, doi:10.1175/1520-0469(1979)036<0437:TSAEOC>2.0.CO;2.

Lenderink, G., and E. van Meijgaard, 2008: Increase in hourly precipitation extremes beyond expectations from temperature changes. *Nat. Geosci.*, **1**, 511–514, doi:10.1038/ngeo262.

Mapes, B., and R. A. Houze, 1993: Cloud clusters and superclusters over the oceanic warm pool. *Mon. Wea. Rev.*, **121**, 1398–1415, doi:10.1175/1520-0493(1993)121<1398:CCASOT>2.0.CO;2.

——, R. Milliff, and J. Morzel, 2009: Composite life cycle of maritime tropical mesoscale convective systems in scatterometer and microwave satellite observations. *J. Atmos. Sci.*, **66**, 199–208, doi:10.1175/2008JAS2746.1.

Merlis, T. M., M. Zhao, and I. M. Held, 2013: The sensitivity of hurricane frequency to ITCZ changes and radiatively forced warming in aquaplanet simulations. *Geophys. Res. Lett.*, **40**, 4109–4114, doi:10.1002/grl.50680.

Muller, C. J., and I. M. Held, 2012: Detailed Investigation of the self-aggregation of convection in cloud-resolving simulations. *J. Atmos. Sci.*, **69**, 2551–2565, doi:10.1175/JAS-D-11-0257.1.

Neelin, J. D., S. Sahany, S. N. Stechmann, and D. Bernstein, 2017: Global warming precipitation accumulation increases above the current-climate cutoff scale. *Proc. Natl. Acad. Sci. USA*, **114**, 1258–1263, doi:10.1073/pnas.1615333114.

O'Gorman, P. A., and T. Schneider, 2009: The physical basis for increases in precipitation extremes in simulations of twenty-first-century climate change. *Proc. Natl. Acad. Sci. USA*, **106**, 14 773–14 777, doi:10.1073/pnas.0907610106.

Otto, F. E. L., N. Massey, G. J. van Oldenborgh, R. G. Jones, and M. R. Allen, 2012: Reconciling two approaches to attribution of the 2010 Russian heat wave. *Geophys. Res. Lett.*, **39**, L04702, doi:10.1029/2011GL050422.

Peters, O., J. D. Neelin, and S. W. Nesbitt, 2009: Mesoscale convective systems and critical clusters. *J. Atmos. Sci.*, **66**, 2913–2924, doi:10.1175/2008JAS2761.1.

——, A. DeLuca, A. Corral, J. D. Neelin, and C. E. Holloway, 2010: Universality of rain event size distributions. *J. Stat. Mech.*, **11**, P11030, doi:10.1088/1742-5468/2010/11/P11030.

——, K. Christensen, and J. D. Neelin, 2012: Rainfall and Dragon-Kings. *Eur. Phys. J. Spec. Top.*, **205**, 147–158, doi:10.1140/epjst/e2012-01567-5.

Quinn, K. M., and J. D. Neelin, 2017: Distributions of tropical precipitation cluster power and their changes under global warming. Part II: Long-term time dependence in Coupled Model Intercomparison Project Phase 5 models. *J. Climate*, **30** (20), 8033–8044, doi:10.1175/JCLI-D-16-0701.1.

Rayner, N. A., D. E. Parker, E. B. Horton, C. K. Folland, L. V. Alexander, D. P. Rowell, E. C. Kent, and A. Kaplan, 2003: Global analyses of sea surface temperature, sea ice, and night marine air temperature since the late nineteenth century. *J. Geophys. Res.*, **108**, 4407, doi:10.1029/2002JD002670.

Seneviratne, S. I., and Coauthors, 2012: Changes in climate extremes and their impacts on the natural physical environment. *Managing the Risks of Extreme Events and Disasters to Advance Climate Change Adaptation*, C. B. Field et al., Eds., Cambridge University Press, 109–230.

Sillmann, J., V. V. Kharin, X. Zhang, F. W. Zwiers, and D. Bronaugh, 2013a: Climate extremes indices in the CMIP5 multimodel ensemble: Part 1. Model evaluation in the present climate. *J. Geophys. Res.*, **118**, 1716–1733, doi:10.1002/jgrd.50203.

——, ——, F. W. Zwiers, X. Zhang, and D. Bronaugh, 2013b: Climate extremes indices in the CMIP5 multimodel ensemble: Part 2. Future climate projections. *J. Geophys. Res.*, **118**, 2473–2493, doi:10.1002/jgrd.50188.

Skok, G., J. Bacmeister, and J. Tribbia, 2013: Analysis of tropical cyclone precipitation using an object-based algorithm. *J. Climate*, **26**, 2563–2579, doi:10.1175/JCLI-D-12-00135.1.

Stauffer, D., and A. Aharony, 1994: *Introduction to Percolation Theory*. 2nd ed. Taylor and Francis, 181 pp.

Stechmann, S. N., and J. D. Neelin, 2011: A stochastic model for the transition to strong convection. *J. Atmos. Sci.*, **68**, 2955–2970, doi:10.1175/JAS-D-11-028.1.

——, and ——, 2014: First-passage-time prototypes for precipitation statistics. *J. Atmos. Sci.*, **71**, 3269–3291, doi:10.1175/JAS-D-13-0268.1.

Sylla, M. B., F. Giorgi, J. S. Pal, P. Gibba, I. Kebe, and M. Nikiema, 2015: Projected changes in the annual cycle of high-intensity precipitation events over West Africa for the late twenty-first century. *J. Climate*, **28**, 6475–6488, doi:10.1175/JCLI-D-14-00854.1.

Tan, J., C. Jakob, W. B. Rossow, and G. Tselioudis, 2015: Increases in tropical rainfall driven by changes in frequency of organized deep convection. *Nature*, **519**, 451–460, doi:10.1038/nature14339.

Tebaldi, C., K. Hayhoe, J. M. Arblaster, and G. A. Meehl, 2006: Going to the extremes: An intercomparison of model-simulated historical and future changes in extreme events. *Climatic Change*, **79**, 185–211, doi:10.1007/s10584-006-9051-4.

TRMM, 2015: Tropical Rainfall Measuring Mission (TRMM) (2011), TRMM (TMPA) rainfall estimate L3 3 hour 0.25 degree × 0.25 degree V7. Goddard Earth Sciences Data and Information Services Center (GES DISC), accessed 1 July 2015. [Available online at https://disc.gsfc.nasa.gov/datacollection/TRMM_3B42_7.html.]

Villarini, G., D. Lavers, E. Scoccimarro, M. Zhao, M. Wehner, G. Vecchi, T. Knutson, and K. Reed, 2014: Sensitivity of tropical cyclone rainfall to idealized global scale forcings. *J. Climate*, **27**, 4622–4641, doi:10.1175/JCLI-D-13-00780.1.

Vizy, E. K., and K. H. Cook, 2012: Mid-twenty-first-century changes in extreme events over northern and tropical Africa. *J. Climate*, **25**, 5748–5767, doi:10.1175/JCLI-D-11-00693.1.

Wang, C.-C., B.-X. Lin, C.-T. Chen, and S.-H. Lo, 2015: Quantifying the effects of long-term climate change on tropical cyclone rainfall using a cloud-resolving model: Examples of two landfall typhoons in Taiwan. *J. Climate*, **28**, 66–85, doi:10.1175/JCLI-D-14-00044.1.

Webster, P. J., G. J. Holland, J. A. Curry, and H.-R. Chang, 2005: Changes in tropical cyclone number, duration, and intensity in a warming environment. *Science*, **309**, 1844–1846, doi:10.1126/science.1116448.

Wehner, M., M. Prabhat, K. A. Reed, D. Stone, W. D. Collins, and J. Bacmeister, 2015: Resolution dependence of future tropical cyclone projections of CAM5.1 in the U.S. CLIVAR Hurricane Working Group idealized configurations. *J. Climate*, **28**, 3905–3925, doi:10.1175/JCLI-D-14-00311.1.

Wing, A. A., and K. A. Emanuel, 2014: Physical mechanisms controlling self-aggregation of convection in idealized numerical modeling simulations. *J. Adv. Model. Earth Syst.*, **6**, 59–74, doi:10.1002/2013MS000269.

——, and T. W. Cronin, 2016: Self-aggregation of convection in long channel geometry. *Quart. J. Roy. Meteor. Soc.*, **142**, 1–15, doi:10.1002/qj.2628.

Wood, R., and P. R. Field, 2011: The distribution of cloud horizontal sizes. *J. Climate*, **24**, 4800–4816, doi:10.1175/2011JCLI4056.1.

Zhao, M., and I. M. Held, 2010: An analysis of the effect of global warming on the intensity of Atlantic hurricanes using a GCM with statistical refinement. *J. Climate*, **23**, 6382–6393, doi:10.1175/2010JCLI3837.1.

——, and ——, 2012: TC-permitting GCM simulations of hurricane frequency response to sea surface temperature anomalies projected for the late-twenty-first-century. *J. Climate*, **25**, 2995–3009, doi:10.1175/JCLI-D-11-00313.1.

——, ——, S. J. Lin, and G. A. Vecchi, 2009: Simulations of global hurricane climatology, interannual variability, and response to global warming using a 50-km resolution GCM. *J. Climate*, **22**, 6653–6678, doi:10.1175/2009JCLI3049.1.

——, ——, and G. A. Vecchi, 2010: Retrospective forecasts of the hurricane season using a global atmospheric model assuming persistence of SST anomalies. *Mon. Wea. Rev.*, **138**, 3858–3868, doi:10.1175/2010MWR3366.1.